Results in Physics 32 (2022) 105133

Contents lists available at ScienceDirect

Results in Physics

journal homepage: www.elsevier.com/locate/rinp

Surface silicon nanostructure for enhancement of blue light absorption

Weishuai Chen [a,b], Jin Tao [a], Hongtao Xu [c], Dan Gao [a], Jinguang Lv [a], Yuxin Qin [a], Guangtong Guo [a,b], Xianglan Li [a,b], Qiang Wang [a], Zhenghua An [c], Jun Zhang [d], Weibiao Wang [a,*], Jingqiu Liang [a,*]

[a] State Key Laboratory of Applied Optics, Changchun Institute of Optics, Fine Mechanics and Physics, Chinese Academy of Sciences, Changchun, Jilin 130033, China
[b] University of Chinese Academy of Sciences, Beijing 100049, China
[c] Fudan Nanofabrication Laboratory, Department of Physics, Fudan University, Shanghai 200433, China
[d] Guangzhou Key Laboratory of Visible Light Communication Engineering Technology, Jinan University, Guangzhou, Guangdong 510632, China

ARTICLE INFO

Keywords:
Silicon
Nanohole-array
Blue light

ABSTRACT

To enhance blue light absorption, a nanohole-array was designed and fabricated on the surface of silicon. The absorptivity of the silicon/nanohole-array composite structure was simulated with the finite-difference time-domain method. The result showed that, when the air filling factor $f = 0.45$, the period $P = 400$ nm, and the hole depth $d = 0.5$ μm, the absorptivity of the silicon was greater than 0.85 in the blue band and the average light absorption gain was about 0.61. A nanohole-array was fabricated with these structural parameters. The experimental results showed that the blue absorptivity of the silicon was greater than 0.91 and the average light absorption gain was about 0.63. For incident light at an angle of 60°, the absorptivity was greater than 0.73 in the blue band. The research demonstrated that the blue light could be absorbed at the deeper position of Si through the nanohole-array. This research may serve as a reference for the design and fabrication of silicon optoelectronic devices with high blue light quantum efficiency.

Introduction

Visible light communication (VLC) is a new type of wireless communication with a spectrum band greater than 400Thz, compared with traditional wireless communication, VLC has richer spectrum resources [1–2]. VLC can effectively alleviate the shortage of spectrum resources in wireless communication [3–5]. VLC has the advantages of no electromagnetic interference, no electromagnetic radiation and high confidentiality, it is an effective alternative when the traditional wireless communication means cannot be used [3]. The emission part of VLC light source is mainly white light LED. White light is usually generated by mixing white LEDs of red, green and blue primaries or phosphors excited by blue LEDs [1], and blue light is the main working wave band of VLC. Silicon (Si) can absorb incident light in the wavelength range 380–1100 nm, therefore the photodetector of VLC system was usually silicon-based photodetector. However, Silicon has a high surface reflectivity (R greater than 38%) and a shallow absorption depth in the blue band, which leads to difficulties in the preparation of high-efficiency silicon blue light detectors. To improve the light absorption of Si is an effective way to improve the quantum efficiency of silicon optoelectronic devices. At present, there are several methods for enhancing light absorption of Si, such as antireflective films [6–9], surface plasmons [10–12], photonic crystals [13], etc. In addition, surface silicon nanostructures, such as nanowires, nanoholes, nanopyramids, and so on, are also used to enhance the light absorption of Si. In 2012, Mavrokefalos et al. [14] fabricated a nanopyramid structure to enhance the light absorption of thin-film solar cells, and the short-circuit current of 10 μm thick plate film was 29.5 mA/cm^2. In 2014, Wu et al. [15] proposed a vertical elliptical silicon nanowire array to achieve broadband absorption by thin-film solar cells, based on the strong mode coupling between adjacent elliptical nanowires, theoretically achieving 29.1% ultimate efficiency. In 2016, Hussein et al. [16] described a funnel-shaped silicon nanostructure with highly efficient light capture because of the large number of leaky mode resonances. In theory, the ultimate efficiency of 41.8% was achieved. In 2017, Zang et al. [17] reported that an inverted pyramid-shaped light trapping structure was

Abbreviations: Silicon, Si; Nanohole, NH-A.

* Corresponding authors at: State Key Laboratory of Applied Optics, Changchun Institute of Optics Fine Mechanics and Physics, Chinese Academy of Sciences, Changchun 130033, China (W. Wang).

E-mail addresses: wangwb@ciomp.ac.cn (W. Wang), liangjq@ciomp.ac.cn (J. Liang).

https://doi.org/10.1016/j.rinp.2021.105133
Received 15 November 2021; Received in revised form 14 December 2021; Accepted 14 December 2021
Available online 16 December 2021

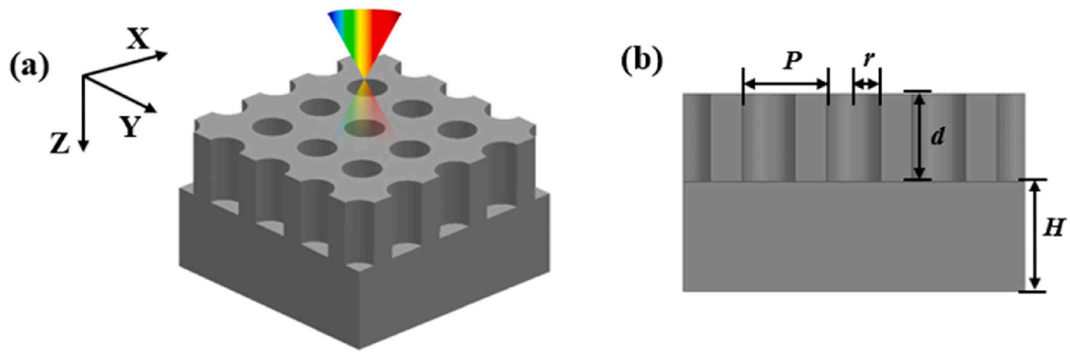

Fig. 1. (a) Structure of the Si/NH-A. (b) Cross section of the Si/NH-A.

prepared on the surface of silicon SPAD, and the photon detection efficiency of the in the near-infrared band is increased by 2.5 times. The same year, Gao et al. [18] fabricated nanohole array structure on the surface of a silicon photodiode and, the quantum efficiency of the device more than 50% in the 820 ~ 860 nm band. In 2018, Deng et al. [19] described an inclined silicon nanohole array for high-efficiency light capture. Due to the unique geometry of the inclined nanohole array, the incident light was reflected back and forth in the array and coupled to the substrate to achieve maximum light capture. Compared with silicon with the same thickness, the short-circuit photocurrent density theoretically increased by 100%. In 2020, Khaled et al. [20] reported a structure with a modified circular silicon nanowire array with crescent-shaped nanoholes. Many modes were excited and coupled with the incident light, so that a high absorption of the incident light was realized. An ultimate efficiency of 32.4% for transverse electric (TE) polarized light and 34.8% for transverse magnetic (TM) polarized light was achieved in theory. In 2021 BARTOLO-PEREZ et al. [21] reported the silicon-based avalanche photodetector which with inverted pyramid-shaped photon trapping structure. The light absorption rate of the device at 850 nm is increased from 16% to 60%, and the external quantum efficiency at 450 nm wavelength is increased from 54% to 82%. These research works mostly focus on enhancing the absorption of Si in the mid-and long-wavelength visible and near-infrared bands, and relatively few research in the blue band. To improve quantum efficiency of silicon optoelectronic devices in blue band, it is necessary to study on the enhancement in the short-wavelength visible band absorption of Si.

In this article, to enhance the blue light absorption of Si, a nanohole-array (NH-A) was designed and fabricated on a Si surface. The finite-difference time-domain (FDTD) numerical algorithm was used to study the influence of NH-As with different structural parameters on the light absorption of Si. A NH-A was fabricated, and the light absorption spectrum of Si/NH-A was measured with the angle-resolved spectrum system in a micro-region, and the experimental results were in good agreement with the numerical results. This research may serve as a reference for the design of high blue light quantum efficiency photodetectors, optical microelectromechanical devices, optical filters, sensors, optical biochemical analysis, etc.

Structure design and simulation setup

To enhance the blue light absorption of Si, a NH-A was designed on the surface of Si. Fig. 1(a) shows the schematic diagram of the Si/NH-A composite structure, and Fig. 1(b) shows the cross-sectional diagram of it. The period of the NH-A was P and the depth of the NH-A was d, where d was much smaller than the thickness of the Si substrate H. The radius of each nanohole was r, which was filled with air, and the filling factor can be expressed as $f = \pi r^2 / P^2$.

Equivalent-medium theory (EMT) and thin-film theory (TFT) are widely combined when designing antireflective gratings [22–24]. According to EMT [25], if the grating period P is much smaller than the incident wavelength λ ($P < \lambda / 10$), the grating will not diffract the light, only zeroth-order reflected waves and zeroth-order transmitted waves will be produced. The effect is similar to that of a layer of homogeneous medium, so that the calculations can be simplified by TFT. For a one-dimensional (1D) subwavelength grating, if $P \ll \lambda$, the zeroth-order equivalent refractive indices of the TE polarization wave and the TM polarization wave for the grating structure can be expressed as:

$$n_{\parallel}^{(0)} = \sqrt{f_1 n_1^2 + (1 - f_1) n_2^2} \tag{1}$$

$$n_{\perp}^{(0)} = \sqrt{\frac{f_1(1 - f_1)(n_1^2 - n_2^2)}{[f_1 n_2^2 + (1 - f_1) n_1^2]}} \tag{2}$$

where f_1 is the filling factor of the material and n_1 is the refractive index of the material in the 1D subwavelength grating. However, in practical applications, fabricating a grating with a period much smaller than the incident wavelength is difficult and expensive, especially for the blue band, which has a short wavelength. If $P \approx \lambda$, Eqs. (1) and (2) are no longer applicable, and a high-order approximation of the equivalent refractive indices is needed. Yeh, Rytov, and others expanded the electromagnetic field in the grating with an eigenmode, obtaining a high-order approximation based on the equivalent theory of the modal method [26–28]. The second-order equivalent refractive indices for the TE and TM modes are then, respectively, expressed as:

$$n_{\parallel}^{(2)} = \left[\left(n_{\parallel}^{(0)}\right)^2 + \frac{\pi^2}{3}\left(\frac{P}{\lambda}\right)^2 f_1^2 (1 - f_1)^2 \left(n_2^2 - n_1^2\right)^2\right]^{1/2} \tag{3}$$

$$n_{\perp}^{(2)} = \left\{\left(n_{\perp}^{(0)}\right)^2\left[1 + \frac{\pi^2}{3}\left(\frac{P}{\lambda}\right)^2 f_1^2 (1 - f_1)^2 \left(n_2^2 - n_1^2\right)^2 \left(n_{\perp}^{(0)}\right)^2 \frac{\left(n_{\perp}^{(0)}\right)^4}{n_1^4 n_2^4}\right]\right\}^{1/2} \tag{4}$$

A 2D square hole subwavelength grating, whose filling factors and periods are equal in both dimensions, can be approximately regarded as the superposition of two 1D gratings with different periodic directions. For any polarization direction of the incident light, the second-order equivalent refractive index of a 2D grating can be approximated as follows [29]:

$$n_{2D-eff}^{(2)} \approx \frac{\overline{n} + 2n_{2D-\parallel}^{(2)} + 2n_{2D-\perp}^{(2)}}{5} \tag{5}$$

where

$$\overline{n} = f_1^2 n_1 + (1 - f_1)^2 n_2 \tag{6}$$

$$n_{2D-\parallel}^{(2)} = \sqrt{f_1 n_1^2 + (1 - f_1) n_{\perp}^{(2)2}} \tag{7}$$

$$n_{2D-\perp}^{(2)} = \sqrt{\frac{n_1^2 n_{\perp}^{(2)2}}{f_1 n_{\parallel}^{(2)2} + (1 - f_1) n_1^2}} \tag{8}$$

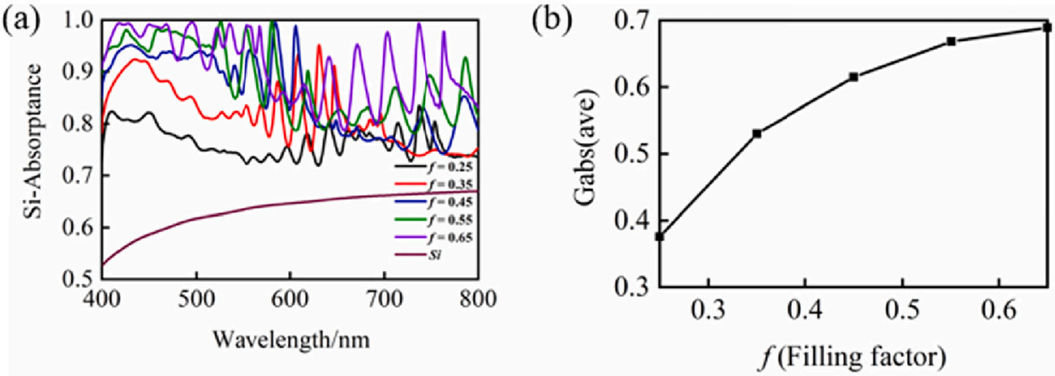

Fig. 2. (a) Light absorption spectra of Si/NH-A in the incident wavelength range 400–800 nm for $P = 400$ nm, $d = 1.0$ μm, and $f = 0.25$, 0.35, 0.45, 0.55, and 0.65. (b) Average light absorption gain of Si/NH-A in the blue band versus *f*.

According to EMT, nanostructures can be regarded as an optical thin film. From TFT, a monolayer antireflective film was prepared based on the following formulas [29]:

$$n_{2D-eff}^{(2)} \approx \sqrt{n_1 n_2} \tag{9}$$

$$2n_{2D-eff}^{(2)} h = (2k+1)\frac{\lambda}{2} \tag{10}$$

where h is the height of the 2D subwavelength grating and the coefficient $k = 0, 1, 2, 3, \dots$

To simplify the calculation, the NH-A structure shown in Fig. 1 was approximately viewed as a 2D square hole subwavelength grating. We take $\lambda = 450$ nm as an example, used Palik's experimental measurement data [30] and Eqs. (1) to (10) to calculate the initial structural parameters of the NH-A that would enhance the absorption of Si in the blue band. The parameters were given as: $P = 400$ nm, $f = 0.55$, and $d = 1.0$ μm. We calculated the influence of the NH-A on the light absorption of Si using the FDTD numerical algorithm based on Maxwell's equations. The calculation settings are as follows: the incident light was a plane wave propagating in the *z* direction and that the wavelength range was 400–800 nm; Periodic boundary conditions were applied to copy the periodic structures in the × and *y* directions; A perfectly matched layer was used to absorb any reflection and transmission fields along the propagation direction, *z*.

Results and discussion

We used $A_{Si} = 1 - T - R$ to determine the light absorption spectrum of Si, where T and R are the transmittance and reflectivity obtained from the FDTD numerical simulation, respectively. We assumed that the substrate of Si was thick enough ($H = 60$ μm), that incident light in the wavelength range 400–800 nm was almost completely absorbed by the Si ($T \approx 0\%$), then the absorptivity A_{Si} of Si could be redefined as: $A_{Si} = 1 - R$. To quantify the improvement in light absorption of Si with the NH-A, we defined the light absorption gain G_{abs} as:

$$G_{abs} = \frac{A_{Si-NH} - A_S}{A_{Si}} \times 100\% \tag{11}$$

To achieve high blue light absorption by Si, the structural parameters of the NH-A (i.e., the filling factor *f*, period *P*, and depth *d*) need to be optimized. The influence of the NH-A with different geometric parameters on Si absorption in air was simulated by the FDTD.

Effect of the NH-A filling factor

Fig. 2(a) and 2(b) show the light absorption spectra of Si/NH-A and the average light absorption gain in the blue band for different filling factors. The period P and the depth d were fixed at 400 nm and 1.0 μm, respectively, and the filling factor f was 0.25, 0.35, 0.45, 0.55, or 0.65. The light absorption spectra shown in Fig. 2(a) were calculated with the FDTD numerical algorithm. As shown in Fig. 2(a). with increasing the filling factor, there were resonance peaks in the Si/NH-A light absorption spectra, which had a narrow full width at half height (FWHM) and a random interval. Unlike Fabry–Perot resonance, these resonance peaks were excited by the coupling between the incident wave and the propagation mode in the array plane, which excited a guided-wave resonance mode [31–33], and excitation of this mode could enhance the absorption of light with less intrinsic absorption in Si [32]. Note that the guided-wave resonance peaks mainly appear in the wavelength range 500–800 nm. In the wavelength range 400–500 nm, there were fewer

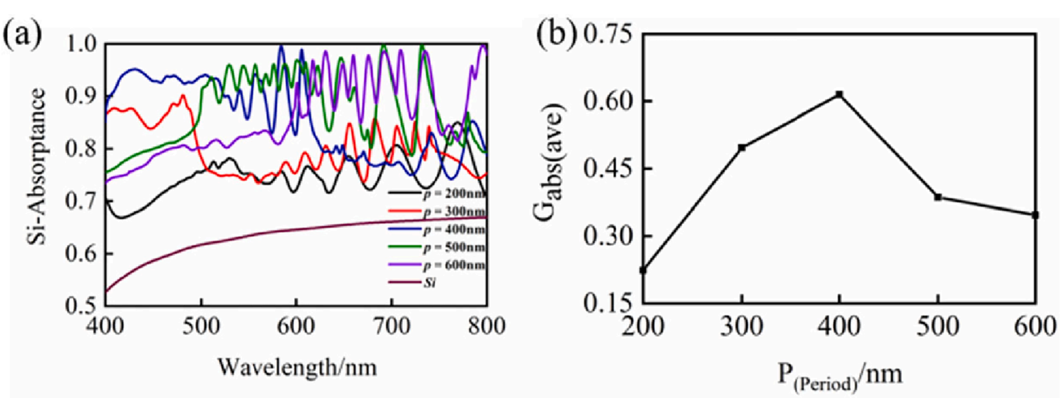

Fig. 3. (a) Light absorption spectra of Si/NH-A in the incident wavelength range 400–800 nm for $f = 0.45$, $d = 1.0$ μm, and $P = 200$, 300, 400, 500, and 600 nm. (b) Average light absorption gain of Si/NH-A in the blue band versus *P*.

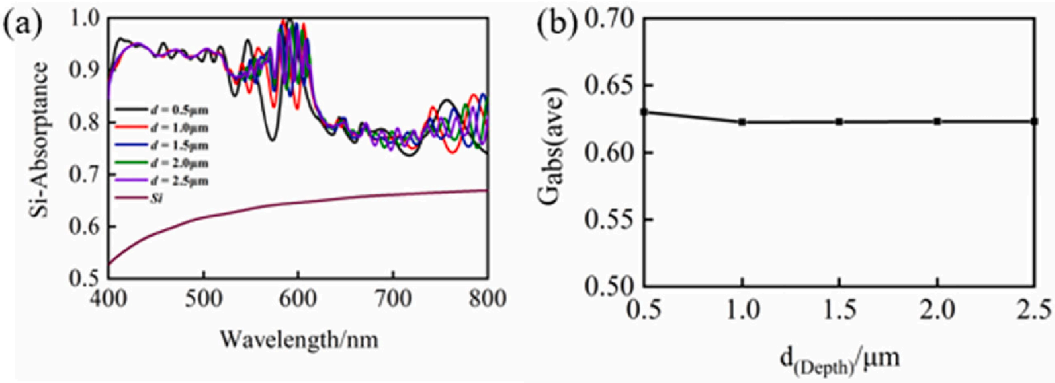

Fig. 4. (a) Light absorption spectra of Si/NH-A in the incident wavelength range 400–800 nm for $f = 0.45$, $P = 400$ nm, and $d = 0.5$, 1.0, 1.5, 2.0, and 2.5 μm. (b) Average light absorption gain of Si/NH-A in the blue band versus *d*.

resonance peaks and the light absorption spectra of Si is relatively smooth, which could be attributed to the large extinction coefficient of Si in this wavelength range, smoothed guided-wave resonance peaks [33–36]. For a larger *f*, there were more resonance peaks, indicating that a larger filling factor can excite more modes [31,37].

Fig. 2(b) shows the dependence of the average light absorption gain $G_{abs(ave)}$ of Si in the blue band on *f*. When the period and hole depth were fixed, the average light absorption increased with an increase of *f*, this phenomenon could be explained as follows: a larger filling factor increases the receiving area of NH-A for the incident light, so the $G_{abs(ave)}$ of Si in the blue band improved. When $f = 0.65$, Si has a higher average light absorption gain in the blue band, but at this time, more guided-wave resonance modes were excited, the light absorption spectrum fluctuation in the blue band was more obvious than for $f = 0.25$, 0.35, 0.45 or 0.55.

Effect of the NH-A period

Fig. 3(a) and 3(b) show the light absorption spectra of Si/NH-A and the average light absorption gain in the blue band for different periods. *f* and *d* were fixed at 0.45 and 1.0 μm, respectively, whereas $P = 200$, 300, 400, 500, or 600 nm. The light absorption spectra of the Si/NH-A shown in Fig. 3(a) were calculated with the FDTD numerical algorithm. It can be seen from Fig. 3(a) that when $P \geq 300$ nm, there are guided-wave resonance peaks in the light absorption spectra. When $P = 500$ or 600 nm, the guided-wave resonance peaks mainly appear in the waveband $P < \lambda < 800$ nm. When $P = 300$ or 400 nm, the guided-wave resonance peaks mainly appear in the 500–800 nm waveband. There are almost no guided-wave resonance peaks in the 400–500 nm waveband. This phenomenon can be attributed to the high extinction coefficient of Si in this band, which smooths the guided-wave resonance peaks. As shown in Fig. 3(a), for $P \geq 400$ nm, when $\lambda \approx P$, the absorptivity of Si increased rapidly due to the strong coupling between the incident light and the NH-A.

The wave vectors β of the guided-wave resonance modes, which are excited by the coupling between vertically incident light and the NH-A, can be expressed as [33,38]:

$$\beta_{(m,n)} = m\frac{2\pi}{p}\widehat{x} + n\frac{2\pi}{p}\widehat{y}, \quad (m, n = 0, \pm1, \pm2, \ldots) \tag{12}$$

where (m, n) are $(\pm1, 0)$ or $(0, \pm1)$, and the corresponding $\beta_{(\pm1,\ 0)}$ and $\beta_{(0,\ \pm1)}$ are the shortest reciprocal lattice vectors. The area enclosed by these vectors corresponds to the first Brillouin zone of the NH-A with a period *P*. This is where the mode energy is most concentrated. For $\lambda \approx P$, the NH-A couples strongly with the incident light, resulting in a rapid increase in the absorptivity of Si. For a NH-A with $P = 200$ nm, there are no guided-wave resonance peaks in the wavelength range 400–800 nm. However, the absorptivity of Si/NH-A was significantly higher than that

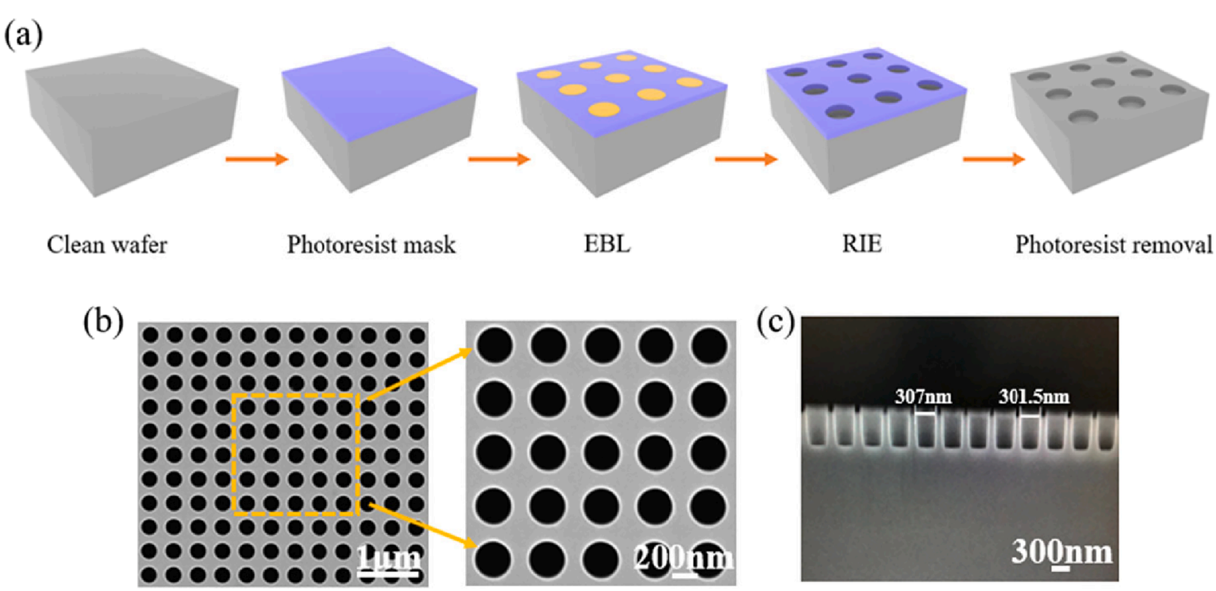

Fig. 5. (a) preparation process of NH-A; Scanning electron micrographs of the NH-A: (b) top view at two magnifications and (c) cross-sectional view.

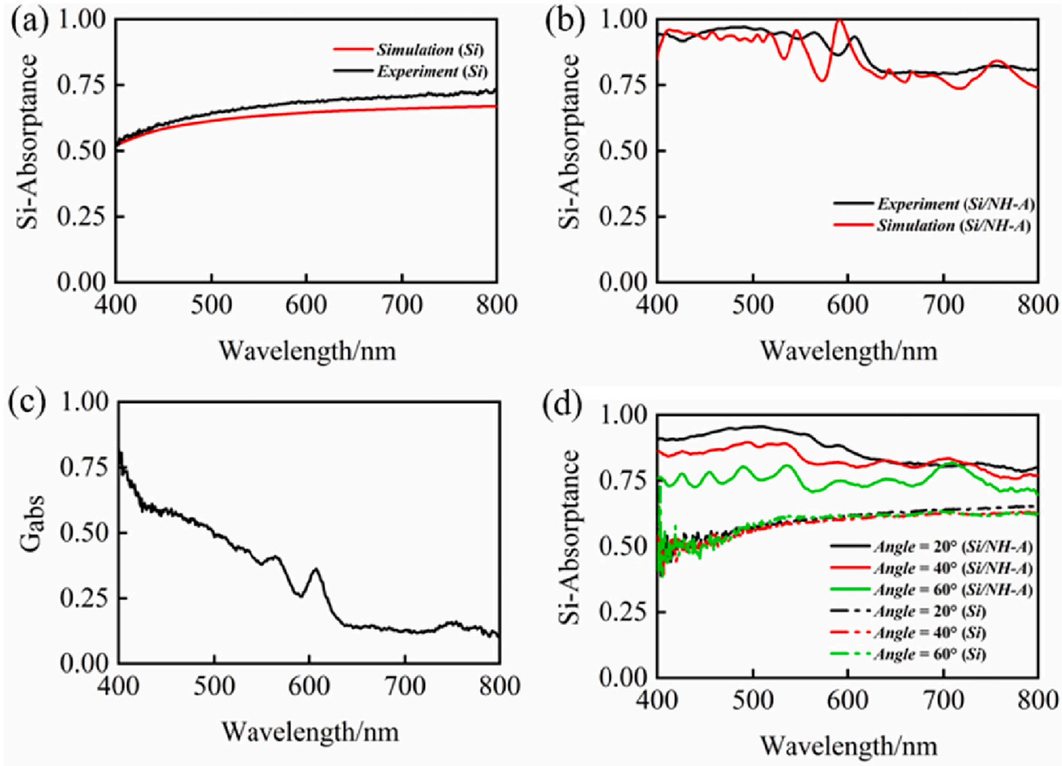

Fig. 6. Comparison of simulated and experimental light absorption spectra of (a) Si and (b) Si/NH-A. (c) Light absorption gain of Si. (d) Comparison of light absorption spectra of Si/NH-A and Si for different angles of incidence.

of Si, and in the wavelength range 500–800 nm the light absorption spectrum of Si/NH-A oscillated in this waveband, which attributed to interference and diffraction of the incident light by the NH-A [35]. Fig. 3 (b) shows the dependence of the average light absorption gain $G_{abs(ave)}$ of Si in the blue band on the period of NH-A. As the period P was increased, $G_{abs(ave)}$ first increased and then decreased. The highest average light absorption gain in the blue band was for $P = 400$ nm.

Effect of the NH-A depth

Fig. 4(a) and 4(b) show the light absorption spectra of Si/NH-A and the average light absorption gain in the blue band for different hole depths. The filling factor f and the period P were fixed at 0.45 and 400 nm, respectively, and the hole depth d was 0.5, 1.0, 1.5, 2.0, or 2.5 μm. The light absorption spectra shown in Fig. 4(a) were calculated with the FDTD numerical algorithm. As shown in Fig. 4(a), with an increase of d, the number of guided-wave resonance peaks increased, indicating that a deeper hole can excite more resonance modes [39]. Fig. 4(b) shows the dependence of the average light absorption gain $G_{abs(ave)}$ in the blue band on the depth of the NH-A. As the hole depth d increased, $G_{abs(ave)} \approx 0.63$ and hardly changed. Due to the large extinction coefficient of Si in the blue band, the light was mainly absorbed by the upper surface of the Si/NH-A and the side wall near the upper surface.

Comparison of numerical and experimental results

From the above research and repeated optimization, $f = 0.45$, $P = 400$ nm, and $d = 0.5$ μm were selected as the structural parameters for the NH-A. We fabricated a NH-A with a square area of 200 μm × 200 μm, by using electron beam lithography (EBL) and reactive ion beam etching (RIE). Fig. 5 (a) shows the basic preparation process of NH-A. The photoresist was prepared using a ZEP520 with a mask thickness of 300 nm, the electron beam lithography (EBL) used a JBX-8100FS machine from JEOL Instrument, and the reactive ion beam etching (RIE) was carried out using the PlasmaPro100 plasma system from Oxford Instruments. Fig. 5(b) show the top view and an enlargement diagram. It can be seen that the NH-A has good uniformity and long-range order. Fig. 5(c) shows cross-sectional diagram of the NH-A. The scanning electron microscopy (SEM) was carried out using an AURIGA-4506 from ZEISS Instruments.

The light absorption spectra of Si and Si/NH-A in the wavelength range 400–800 nm were measured using an angle-resolved spectrum system in a micro-region (ARM) from Idea &Optics. The experimental results were compared with the numerical results based on FDTD. Fig. 6 (a) and 6(b) compare the numerical light absorption spectra (red lines) with the experimental results (black lines) for Si and Si/NH-A, respectively. The absorption rate of Si/NH-A in the blue band $A_{Si\text{-}NH}$ greater than 0.91, so that the NH-A effectively enhanced the blue absorption of Si. It can be seen from Fig. 6(a) that for Si, the measurements were higher than the numerical results in the wavelength range 400–800 nm, but the trends were the same, since as the wavelength increased, the absorptivity gradually increased. Fig. 6(b) shows that compared with simulation, the resonance peak had shifted, and moreover some of the small oscillations in the numerical results do not appear in the experimental data. These differences between the numerical and experimental results as shown in Fig. 6(a) and 6(b) may be due to the following reasons: (1) There were measurement errors during the experiment. (2) The sample have errors in the processing, as shown in Fig. 6(b) [40]. Fig. 6(c) shows the actual light absorption gain of Si in the wavelength range 400–800 nm, which was calculated from the experimental results shown in Fig. 6(a) and 6(b) using Eq. (11). The light absorption gain of Si in the blue band was between 0.45 and 0.8, and the average light absorption gain of Si in this band was $G_{abs(ave)} \approx 0.63$.

For practical applications, it is necessary to consider that how much light is absorbed by the Si/NH-A when the angle of incidence is not perpendicular. Thus, we measured the absorptivity of Si/NH-A and Si with incident angles of 20°, 40°, and 60° in the wavelength range 400–800 nm, as shown in Fig. 6(d). As the incident angle increased, the

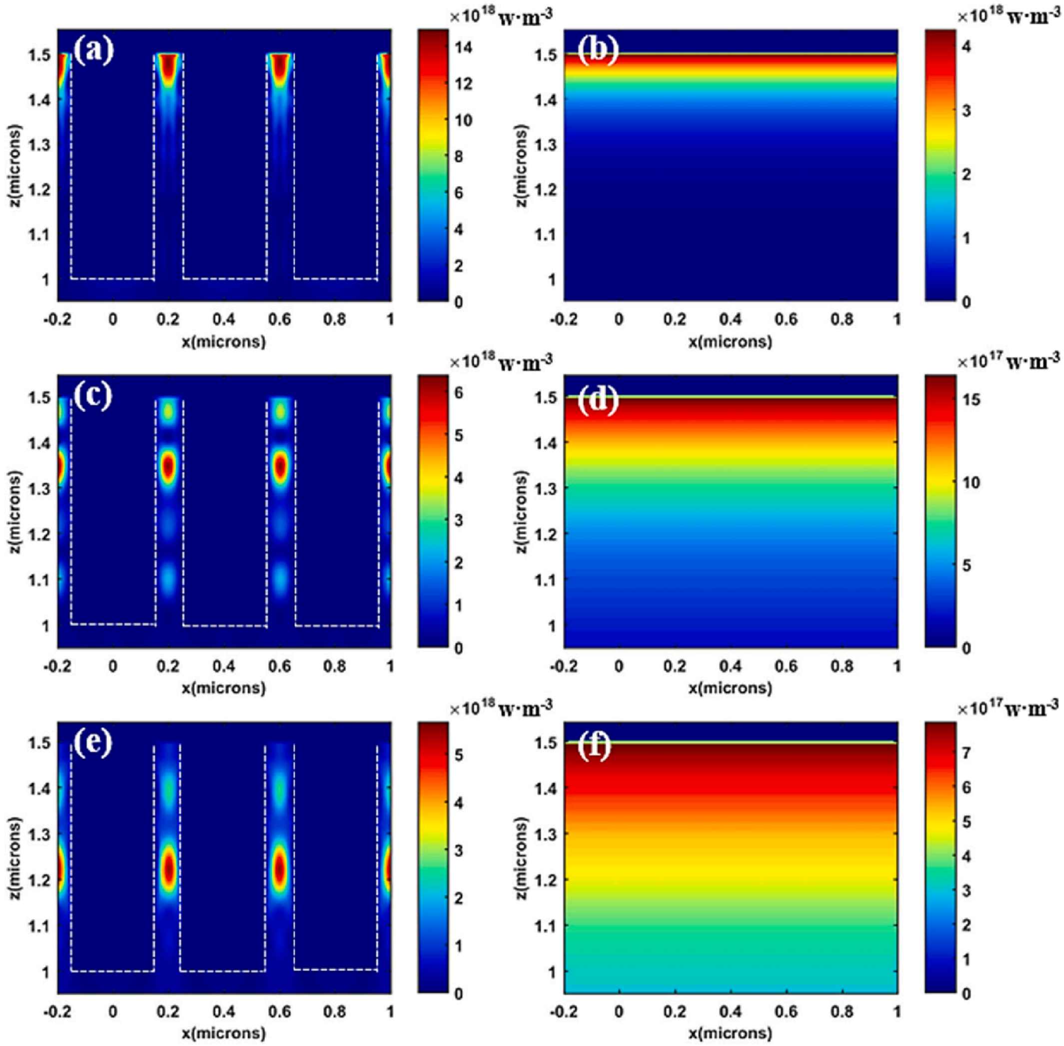

Fig. 7. Light absorption distribution: (a) Si/NH-A for λ = 400 nm, (b) Si for λ = 400 nm, (c) Si/NH-A for λ = 450 nm, (d) Si for λ = 450 nm, (e) Si/NH-A for λ = 500 nm, and (f) Si for λ = 500 nm. The color bars indi-cate the light absorbed per unit volume.

light absorption spectra of Si were almost unchanged, whereas the absorptivity of Si/NH-A in the blue band gradually decreased. For light incident at an angle of 60°, the absorptivity greater than 0.73 in the blue band. For the other bands, the absorptivity greater than 0.7. This means that for light incident at a large angle, the NH-A can still enhance light absorption in the range of 400–800 nm.

Effect of NH-A on the blue absorption distribution

Si has a larger absorption coefficient in the blue band and a smaller absorption depth. The effect of NH-A on the blue absorption distribution of Si was studied for λ = 400, 450, and 500 nm. Along z direction, the light absorption distributions of Si/NH-A and Si were calculated with the FDTD numerical method. Fig. 7(a) and 7(b) show the light absorption distribution of Si/NH-A and Si when λ = 400 nm. Fig. 7(c) and 7(d) show the light absorption distribution of Si/NH-A and Si when λ = 450 nm. Fig. 7(e) and 7(f) show the light absorption distribution of Si/NH-A and Si when λ = 500 nm. As the wavelength increased, the light absorption depth of Si/NH-A and Si gradually increased, which can be attributed to the gradual decrease of the extinction coefficient of Si with an increase of the incident wavelength.

Fig. 8(a)–8(c) show for λ = 400, 450, and 500 nm, respectively, the normalized light absorption intensity and the corresponding gradient as a function of the transmission distance of normal incident light for Si/NH-A and Si. As the transmission distance increased, the normalized light absorption intensity for both Si/NH-A and Si had an upward trend, and the light absorption intensity of Si/NH-A was always greater than that of Si, further, as the transmission distance increased, the gradients for both Si/NH-A and Si became smaller. For the same transmission distance, the gradient for Si/NH-A was obviously greater than for Si, indicating that more incident light was absorbed inside the Si/NH-A, the blue light can be absorbed at the deeper position of Si through the NH-A.

Conclusion

The enhancement of blue light absorption of Si by NH-A was verified by simulations and experiments in this article. Based on the FDTD numerical calculations and repeated optimization, the structural parameters of NH-A were selected as $f = 0.45$, $P = 400$ nm, and $d = 0.5$ μm. A NH-A was fabricated with these structural parameters, according to the experimental results, the absorptivity of Si/NH in the blue band was $A_{Si\text{-}NH}$ greater than 0.91 and the average light absorption gain $G_{abs\ (ave)} \approx 0.63$. The results showed that the Si/NH-A composite structure still had a high absorption for light incident at an angle of 60°, as in the blue band, $A_{Si\text{-}NH}$ greater than 0.73. The FDTD numerical algorithm was used to calculate the light absorption distribution of Si/NH-A and in the blue band. The result shows that more light was absorbed inside the Si/NH-A, the blue light can be absorbed at the deeper position of Si through the

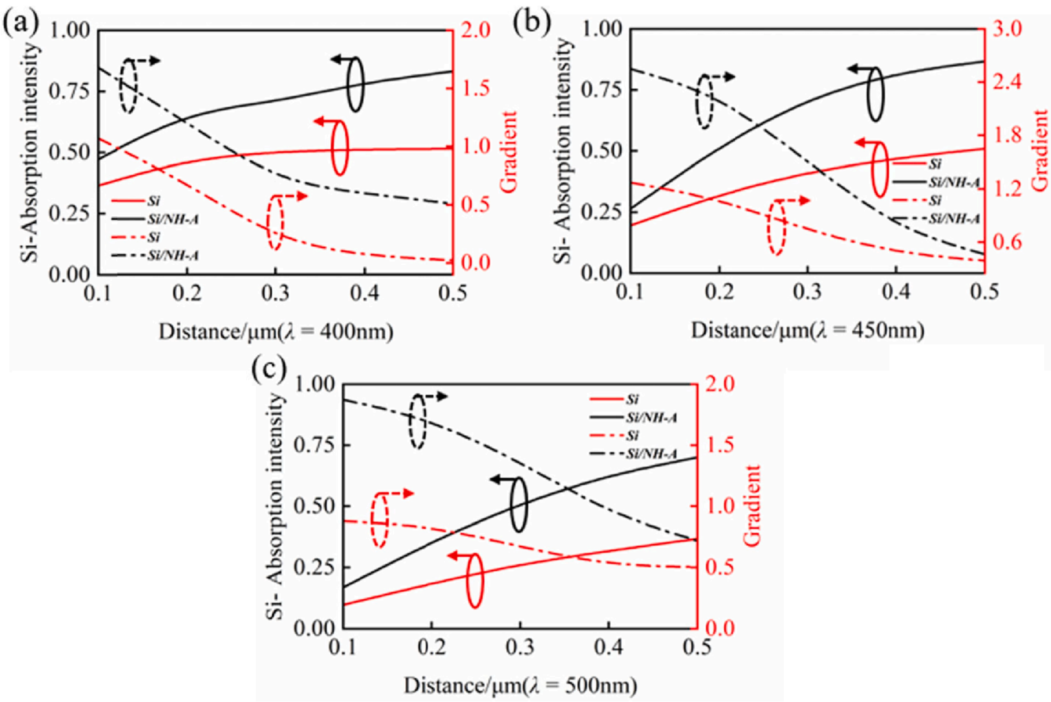

Fig. 8. Normalized light absorption intensity for Si/NH-A (black line) and Si (red line) and the corresponding gradient (dotted lines): (a) λ = 400 nm, (b) λ = 450 nm, and (c) λ = 500 nm. Distance represent light transmission distance. The black lines (Si/NH-A) and red lines (Si) with moving arrow pointing to the left coordinate represent the normalized absorption intensity change with transmission distance. The black dotted lines (Si/NH-A) and red dotted lines (Si) with moving arrow pointing to the right coordinate represent the gradient change with transmission distance, which corresponding to the change of normalized light absorption intensity.

NH-A. This research can serve as a reference for the design and fabrication of silicon optoelectronic devices with a high quantum efficiency for blue light.

Funding

This research received funding from the National Key Research and Development Program (2018YFB1801902 and 2018YFB1801901) and the Jilin Province Science and Technology Development Program Project (20190302062GX) and Youth Project of National Natural Science Foundation of China (NSFC):(12004139) and the Science and Technology Plan of Guangdong Province program Project (2016B010111003).

CRediT authorship contribution statement

Weishuai Chen: Writing – original draft, Conceptualization, Methodology. **Jin Tao:** Conceptualization, Investigation. **Hongtao Xu:** Resources. **Dan Gao:** Software. **Jinguang Lv:** Formal analysis. **Yuxin Qin:** Validation. **Guangtong Guo:** Investigation. **Xianglan Li:** Investigation. **Qiang Wang:** Project administration. **Zhenghua An:** Resources. **Jun Zhang:** Project administration, Formal analysis. **Weibiao Wang:** Writing – review & editing, Conceptualization. **Jingqiu Liang:** Writing – review & editing, Supervision.

Declaration of Competing Interest

The authors declare that they have no known competing financial interests or personal relationships that could have appeared to influence the work reported in this paper.

References

[1] Gao D, Zhang J, Wang F, Liang JQ, Wang WB. Design and simulation of ultra-thin and high-efficiency silicon-based trichromatic PIN photodiode arrays for visible light communication. Opt. Commun. 2020;475:126296. https://doi.org/10.1364/OFC.2015.Tu2G.5.

[2] Minotto A, Haigh PA, Ukasiewicz UG, Lunedei E, Cacialli F. Visible light communication with efficient far-red/near-infrared polymer light-emitting diodes. Light-Sci. Appl. 2020;9(1):70. https://doi.org/10.1038/s41377-020-0314-z.

[3] M. Seminara, M. Meucci, F. Tarani, C. Riminesi, and J.Catani, " Characterization of a vlc system in real museum scenario using diffusive led lighting of artworks," Photonics Res. vol. 9, no. 4, (2021), pp. 548-557, 10.1364/PRJ.414394.

[4] Nazari Z, Zvanovec S, Ghassemlooy Z, Eldeeb HB, Uysal M. Coverage of a shopping mall with a flexible oled-based visible light communications. Opt. Express 2020;28 (7):10015–26. https://doi.org/10.1364/OE.389814.

[5] Zhen C, Fang J, Jiang ZL, Yu X, Zhe C. A Physical-Layer Secure Coding Scheme for Indoor Visible Light Communication Based on Polar Codes. IEEE Photonics J 2017; 10(5):1–13. https://doi.org/10.1109/JPHOT.2018.2869931.

[6] Maniyara RA, Mkhitaryan VK, Chen TL, Ghosh DS, Pruneri V. An antireflection transparent conductor with ultralow optical loss (<2 %) and electrical resistance (<6 Ω sq^{-1}). Nat. Commun. 2016;7:13771. https://doi.org/10.1038/ncomms13771.

[7] Hou G, García I, Rey-Stolle I. High-low refractive index stacks for broadband antireflection coatings for multijunction solar cells. Sol. Energy 2021;217:29–39. https://doi.org/10.1016/j.solener.2021.01.060.

[8] Guo M, Yi K, Cui X, Shao S, Hu G, Zhao J, et al. Design and preparation of UV-visible-shortwave near infrared cut-off and mid-infrared antireflection coating. Optik 2021;227:165470. https://doi.org/10.1016/j.ijleo.2020.165470.

[9] S. A. Boden and D. M. Ba Gnall, "Sunrise to sunset optimization of thin film antireflective coatings for encapsulated, planar silicon solar cells," Prog. Photovolt. Res. Appl. 17, (2010), pp. 241-252, 10.1002/pip.884.

[10] Kumawat UK, Kumar K, Mishra S, Dhawan A. Plasmonic enhanced microcrystalline silicon solar cells. J. Opt. Soc. Am. B 2020;37:495–504. https://doi.org/10.1364/JOSAB.378946.

[11] Olaimat MM, Yousefi L, Ramahi O. Using plasmonics and nanoparticles to enhance the efficiency of solar cells: Review of latest technologies. J. Opt. Soc. Am. B 2021; 38:638–51. https://doi.org/10.1364/JOSAB.411712.

[12] Alkhalayfeh MA, Aziz AA, Pakhuruddin MZ. An overview of enhanced polymer solar cells with embedded plasmonic nanoparticles. Renew. Sust. Energ. Rev. 2021; 141:110726. https://doi.org/10.1016/j.rser.2021.110726.

[13] Tanaka Y, Kawamoto Y, Fujita M, Noda S. Enhancement of broadband optical absorption in photovoltaic devices by band-edge effect of photonic crystals. Opt. Express 2013;21:20111–8. https://doi.org/10.1364/OE.21.020111.

[14] Mavrokefalos A, Han SE, Yerci S, Branham MS, Chen G. Efficient light trapping in inverted nanopyramid thin crystalline silicon membranes for solar cell applications. Nano Lett. 2012;12:2792. https://doi.org/10.1021/nl2045777.

[15] Wu Y, Xia Z, Liang Z, Jian Z, Qin X. Broadband absorption enhancement in elliptical silicon nanowire arrays for photovoltaic applications. Opt. Lett. 2014;22 (Suppl 5):A1292. https://doi.org/10.1364/OE.22.0A1292.
[16] Hussein M, Hameed M, Areed N, Yahia A, Obayya S. Funnel-shaped silicon nanowire for highly efficient light trapping. Opt. Lett. 2016;41:1010. https://doi.org/10.1364/OL.41.001010.
[17] Zang K, Jiang X, Huo Y, et al. Silicon single-photon avalanche diodes with nano-structured light trapping[J]. Nat Commun 2017;8(1):1–6. https://doi.org/10.1038/s41467-017-00733-y.
[18] Gao Y, Cansizoglu H, Polat KG, et al. Photon-trapping microstructures enable high-speed high-efficiency silicon photodiodes[J]. Nat Photonics 2017;11(5):301–8. https://doi.org/10.1038/nphoton.2017.37.
[19] Deng C, Tan X, Jiang L, Tu Y, Ye M, Yi Y. Efficient light trapping in silicon inclined nanohole arrays for photovoltaic applications. Opt. Commun. 2018;407:199–203. https://doi.org/10.1016/j.optcom.2017.09.016.
[20] Khaled A, Hussein M, Hameed M, Rahman A, Obayya S. Characteristics of silicon nanowire solar cells with crescent nanohole. Opt. Express 2020;28:31020–33. https://doi.org/10.1364/OE.397051.
[21] Bartolo-Perez C, Chandiparsi S, Mayet AS, et al. Avalanche photodetectors with photon trapping structures for biomedical imaging applications[J]. Opt. Express 2021;29(12):19024–33. https://doi.org/10.1364/OE.421857.
[22] Gaylord TK, Baird WE, Moharam MG. Zero-reflectivity high spatial-frequency rectangular-groove dielectric surface-relief gratings. Appl. Optics 1986;25:4562. https://doi.org/10.1364/AO.25.004562.
[23] Perl EE, McMahon WE, Farrell RM, Denbaars SP, Speck JS, Bowers JE. Surface structured optical coatings with near-perfect broadband and wide-angle antireflective properties. Nano Lett. 2014;14:5960. https://doi.org/10.1021/nl502977f.
[24] Ding H, Liu D, Li B, Wang Z, Ren L. Broader-band and flexible antireflective films with the window-like structures inspired by the backside of butterfly wing scales. ACS Appl. Mater. Interfaces 2021;13:19450–9. https://doi.org/10.1021/acsami.1c01352.
[25] Brundrett DL, Glytsis EN, Gaylord TK. Homogeneous layer models for high-spatial-frequency dielectric surface-relief gratings: Conical diffraction and antireflection designs. Appl. Optics 1994;33:2695–706. https://doi.org/10.1364/AO.33.002695.
[26] Yariv A, Yeh P. Electromagnetic propagation in periodic stratified media. II. Birefringence, phase matching, and x-ray lasers. J. Opt. Soc. Am. 1977;67:438–47. https://doi.org/10.1364/JOSA.67.000438.
[27] Yeh P, Yariv A, Hong CS. Electromagnetic propagation in periodic stratified media. I. General theory. J. Opt. Soc. Am. 1977;67:423–38. https://doi.org/10.1364/JOSA.67.000423.
[28] Rytov SM. Electromagnetic properties of a finely stratified medium. Sov. Phys. JEPT 1956;2:466–75.
[29] Bruer R, Bryngdahl O. Design of antireflection gratings with approximate and rigorous methods. Appl. Optics 1994;33:7875–82. https://doi.org/10.1364/AO.33.007875.
[30] Palik ED. Handbook of optical constants of solids. Academic Press 1985:547–52.
[31] Du QG, Chan HK, Demir HV, Hong YY, Sun XW. Enhanced optical absorption in nanopatterned silicon thin films with a nano-cone-hole structure for photovoltaic applications. Opt. Lett. 2011;36:1713–5. https://doi.org/10.1364/OL.36.001713.
[32] Sturmberg B, Dossou KB, Botten LC, Asatryan AA, McPhedran RC. Modal analysis of enhanced absorption in silicon nanowire arrays. Opt. Express 2011;19(Suppl 5):A1067. https://doi.org/10.1364/OE.19.0A1067.
[33] Donnelly JL, Sturmberg B, Dossou KB, Botten LC, Asatryan AA, Poulton CG, et al. Mode-based analysis of silicon nanohole arrays for photovoltaic applications. Opt. Express 2014;22(Suppl 5):A1343. https://doi.org/10.1364/OE.22.0A1343.
[34] Fan S, Joannopoulos JD. Analysis of guided resonances in photonic crystal slabs. Phys. Rev. B 2002;65:235112. https://doi.org/10.1103/PhysRevB.65.235112.
[35] Hu L, Chen G. Analysis of optical absorption in silicon nanowire arrays for photovoltaic applications. Nano Lett. 2007;7:3249–52. https://doi.org/10.1021/nl071018b.
[36] Fang X, Zhao CY, Bao H. Radiative behaviors of crystalline silicon nanowire and nanohole arrays for photovoltaic applications. J. Quant. Spectrosc. Radiat. Transf. 2014;133:579–88. https://doi.org/10.1016/j.jqsrt.2013.09.021.
[37] Li L, Peng KQ, Bo H, Xin W, Hu Y, Wu XL, et al. Broadband optical absorption enhancement in silicon nanofunnel arrays for photovoltaic applications. Appl. Phys. Lett. 2012;100:16986. https://doi.org/10.1063/1.4723850.
[38] Peng S, Morris GM. Resonant scattering from two-dimensional gratings. J. Opt. Soc. Am. 1996;13:993. https://doi.org/10.1364/JOSAA.13.000993.
[39] Wang W, Zhang J, Zhang Y, Xie Z, Qin G. Optical absorption enhancement in submicrometre crystalline silicon films with nanotexturing arrays for solar photovoltaic applications. J. Phys. D Appl. Phys. 2013;46:195106. https://doi.org/10.1088/0022-3727/46/19/195106.
[40] Zhengji XU, Li N, Dong Y, Fu YH, Singh N. Metasurface-based subtractive color filter fabricated on a 12-inch glass wafer using CMOS platform. Photonics Res. 2021;9(1):13–20. https://doi.org/10.1364/PRJ.404124.